Graphitic carbon nitride/SmFeO 3 composite Z-scheme photocatalyst with high visible light activity

Bilel Chouchene, Thomas Gries, Lavinia Balan, Ghouti Medjahdi, Raphaël Schneider

Graphitic carbon nitride/$SmFeO_3$ composite Z-scheme photocatalyst with high visible light activity

Bilel Chouchene[1,2], Thomas Gries[2], Lavinia Balan[3], Ghouti Medjahdi[2] and Raphaël Schneider[1]

[1] Université de Lorraine, CNRS, LRGP, F-54000 Nancy, France

[2] Université de Lorraine, CNRS, IJL, F-54000 Nancy, France

[3] CEMHTI-UPR 3079 CNRS, Site Haute Température, 1D avenue de la Recherche Scientifique, 45071 Orléans, France

E-mail: raphael.schneider@univ-lorraine.fr

Abstract

In this work, novel heterostructured photocatalysts associating graphitic carbon nitride (g-CN) and $SmFeO_3$ were prepared via a mixing-ultrasonication process. Structural, optical and morphological characterizations demonstrate that the interfacial junction between g-CN and SmFeO3 is well established for all g-CN/SmFeO3 composites prepared with g-CN:$SmFeO_3$ weight ratio of 20:80, 50:50 and 80:20. The g-CN/$SmFeO_3$ (80:20) composite exhibits the highest photocatalytic activity for the degradation of pollutants like the Orange II dye and the tetracycline hydrochloride antibiotic under visible light irradiation. This high photocatalytic activity originates from the enhanced light absorption over the whole visible region compared to pure g-CN and from the improved separation and transfer of photogenerated electron/hole pairs as demonstrated by photoluminescence and photocurrent measurements. A Z-scheme charge carrier transfer mechanism was demonstrated for the photocatalytic reactions. The g-CN/$SmFeO_3$ (80:20) catalyst was also demonstrated to be stable and can be reused up to six times without significant alteration of the activity.

Keywords: graphitic carbon nitride; $SmFeO_3$; heterostructured photocatalyst; pollutant photodegradation; Z-scheme mechanism

1. Introduction

Graphitic carbon nitride (g-CN) is a layered π-conjugated polymeric n-type semiconductor that has recently gained considerable attention for various photocatalytic applications like pollutant degradation, hydrogen production and CO_2 reduction [1-4]. g-CN is easily synthesized by the polymerization of nitrogen-rich organic precursors like melamine, urea or dicyandiamide, and exhibits good thermal and chemical stability and a low cytotoxicity. Moreover, the bandgap energy of g-CN is of ca. 2.7 eV enabling photocatalytic reactions to be conducted in the visible range until ca. 460 nm [1-4]. The conduction band edge potential of g-CN is located at -1.34 eV vs NHE, which confers to g-CN a marked photocatalytic reducing ability. However, the photocatalytic activity of g-CN is hampered by its low quantum efficiency which originates from the weak charge mobility and from the fast charge carriers recombination [1-4].

In recent years, various strategies have been developed to overcome these challenges including the building of g-CN-based heterostructured photocatalysts associating g-CN and another semiconductor [5-10], the doping of g-CN with non-metal (P, B, S,…) [11-13] or metal (Mn^{2+}, Cu^{2+}, Co^{3+},…) elements [14-16], the hybridization and sensitization of g-CN with macrocyclic heterocycles [17] or the modification of g-CN structural and textural properties, for example by intercalation [18-20]. When considering the engineering of heterostructured photocatalysts, the use of perovskite type oxides and especially of ABO_3 materials (where A is a rare-earth element or alkaline-earth metal and B is a transition metal element) has received high interest due to their high stability, excellent physico-chemical properties and to their narrow bandgap that allows their activation by visible light [21]. Recently, perovskites like $LaMO_3$ (M = Fe, Mn, Co, Ni or Ti) or $MTiO_3$ (M = Sr or Ca) were associated to g-CN to improve the charge carriers delocalization and these photocatalysts were successfully used for water splitting or pollutants degradation [22-29].

Among rare-earth orthoferrites, the $SmFeO_3$ p-type semiconductor is of high potential for photocatalytic applications due to its optical bandgap that can be reduced up 2.01 eV allowing the absorption of light up to ca. 600 nm [30-32]. However, $SmFeO_3$ has only scarcely been used in photocatalysis due to its low specific surface area like most perovskite-

type oxides [33] and to the fast recombination of photogenerated electron-hole pairs upon light activation [30, 32, 34, 35].

In this paper, a new solvothermal method followed by a calcination was first developed for the preparation of orthorhombic $SmFeO_3$ nanoparticles with an average diameter of 19 nm using $Sm(NO_3)_3$ and $Fe(NO_3)_3$ as precursors. Next, $SmFeO_3$ particles were associated to g-CN sheets using a mixing-sonication process to produce g-CN/$SmFeO_3$ composites. The g-CN:$SmFeO_3$ ratio was varied and the highest photocatalytic activity under visible light irradiation for the degradation of the Orange II dye and of the tetracycline hydrochloride antibiotic was observed for the g-CN/$SmFeO_3$ (80:20) composite. Our results demonstrate that the g-CN/$SmFeO_3$ composite exhibits a significantly improved photocatalytic activity compared to pure g-CN due to the improved transfer and separation of charge carriers and to the enhanced visible light absorption. Based on reactive species trapping experiments, a Z-scheme photogenerated electrons transfer mechanism based on p-n heterojunction was demonstrated for the reactions mediated by the g-CN/$SmFeO_3$ catalyst.

2. Experimental section

2.1. Materials

Samarium (III) nitrate hexahydrate (99.9%, Sigma), iron (III) nitrate nonahydrate, (99%, Sigma), citric acid (99.5%, Sigma), ammonium hydroxide solution (28%, Alpha Aesar), melamine (99.9%, Sigma) and anhydrous ethanol were of analytical grade and were used without further purification. All solutions were prepared using Milli-Q water (18.2 MΩ.cm, Millipore) as solvent.

2.2. Synthesis of $SmFeO_3$ nanoparticles

$SmFeO_3$ was synthesized by a solvothermal method followed by a calcination. Briefly, $Sm(NO_3)_3$ (5 mmol, 2.222 g), $Fe(NO_3)_3$ (5 mmol, 2.020 g) and citric acid (10 mmol, 1.920 g) were dissolved in an ethanol/water (2:1, 30 mL) mixture and the pH of the solution was adjusted to 7 using ammonium hydroxide. The solution was stirred for 30 min at room temperature, subsequently transferred into a 100 mL Teflon-sealed autoclave and heated at 180°C for 12 h. After cooling, the $SmFeO_3$ precursor was recovered by centrifugation (15

min, 4000 rpm), washed with water (2 x 40 mL), with absolute ethanol (2 x 40 mL) and dried at 70°C overnight. Finally, the green precursor was calcined under air at 600°C for 2 h using a heating rate of 10°C.min^{-1} to obtain $SmFeO_3$ nanoparticles.

2.3. Synthesis of bulk g-CN

Bulk g-CN was prepared by thermal condensation of melamine. In a typical experiment, melamine (5 g) was placed in a crucible with a cover and heated at 500°C for 2 h using a heating rate of 10 °C.min^{-1}. The yellow powder obtained was grounded using an agate mortar before use.

2.4. Synthesis of g-CN/$SmFeO_3$ catalysts

The g-CN/$SmFeO_3$ catalysts were synthesized through a mixing-ultrasonic method. In a typical experiment, appropriate amounts of $SmFeO_3$ and g-CN were separately dispersed in 50 mL of distilled water under sonication for 60 min. Then, the solutions were mixed and further sonicated for 90 min. The solid was recovered by centrifugation (4000 rpm for 15 min), washed with water (2 x 40 mL), with absolute ethanol (2 x 40 mL) and dried for 12 h at 70°C. The loading in g-CN was varied to prepare catalysts containing 20, 50, and 80 wt% g-CN relative to $SmFeO_3$.

2.5. Visible light photocatalytic activity

The photocatalytic activity of the g-CN/$SmFeO_3$ catalysts was evaluated in the photo-degradation of the Orange II dye and of tetracycline hydrochloride, both used at a 10 mg.L^{-1} concentration. Experiments were conducted under visible light irradiation using a 300 W Osram lamp equipped with UV cut-off filter ($\lambda > 400$ nm). The light intensity used was 15 mW.cm^{-2}. In a typical experiment, 30 mg of photocatalyst were dispersed in 30 mL of the pollutant aqueous solution and the suspension was stirred in the dark for 30 min to reach the adsorption-desorption equilibrium between the photocatalyst and the pollutant. Then the mixture was exposed to light irradiation. At a given irradiation time interval, 2 mL of the mixture were removed, centrifuged for 2 min at 15000 rpm to remove the photocatalyst and the photodegradation was monitored by UV-visible spectroscopy at the wavelength of 485 nm for Orange II and 356 nm for tetracycline hydrochloride.

2.6. Characterization

The crystal structures of the synthesized powders were determined by X-ray diffraction (XRD) using a Panalytical X'Pert pro MPD diffractometer using Cu Kα radiation (wavelength of 1.5405 Å). The morphology and the microstructure of g-CN/$SmFeO_3$ catalysts were investigated by scanning electron microscopy (SEM, JEOL, JSM-6490 LV) and transmission electron microscopy (TEM) (Philips CM200 instrument operating at 200 KV).

X-ray photoelectron spectroscopy (XPS) measurements were carried out with a Gammadata Scienta SES 200-2 spectrometer. The CASAXPS software (Casa Software Ltd, Teignmouth, UK, www.casaxps.com) was used for all peak fitting procedures and the areas of each component were determined according to classical Scofield sensitivity factors. Thermogravimetric analyses (TGA) were conducted using the TGA/DSC STARe (Mettler Toledo) equipment from 35°C to 1000°C at a heating rate of 10 °C.min^{-1} under O_2 atmosphere with a flow rate of 50 mL.min^{-1}. N2 adsorption-desorption isotherms were measured at -196°C on a Micromeritics ASAP 2420 equipment. Before analysis, the samples were degassed at 150°C for 12 h. The value of the specific surface area was determined by the Brunauer-Emmett-Teller (BET) method.

The optical measurements were performed at room temperature under ambient conditions. A Bruker ALPHA spectrometer was used to record the Fourier transform infrared (FT-IR) spectra in the range of 400-4000 cm^{-1}. UV-visible absorption spectra were recorded using a Thermo Scientific Evolution 220 UV-visible spectrometer. UV-visible diffuse reflectance spectra were recorded using a Shimadzu 2600-2700 UV-visible spectrometer. Photoluminescence (PL) emission spectra were recorded on a Horiba Fluoromax-4 Jobin Yvon spectrofluorimeter.

The surface charge of the prepared materials was obtained using Zetasizer Nano Zs (Malvern Instruments). Typically, 20 mg of the sample was dispersed in 50 mL of distilled water under sonication at room temperature. The pH of the solutions was adjusted with 0.1 M HCl and 0.1 M NaOH solutions before measurement.

The electrochemical measurements were carried out in a quartz beaker using SP150 Biologic potentiostat with a standard mode with three electrodes. An 0.1 M aqueous solution of

Na_2SO_4 was used as electrolyte. For the working electrode, 2 mg of photocatalyst was dispersed in 250 µl of DMF and then deposited on a FTO glass with an area of 2 cm^2. After being heated for 2 h at 150°C to remove DMF, a homogeneous film was obtained. A platinum wire and an Ag/AgCl electrode were used as counter electrode and reference electrode, respectively.

3. Results and discussion

3.1. Synthesis and characterization of g-CN/$SmFeO_3$ composites

$SmFeO_3$ nanoparticles were prepared using a solvothermal process using $Sm(NO_3)_3$ and $Fe(NO_3)_3$ as precursors followed by calcination at 600°C. Next, $SmFeO_3$ and g-CN particles were mixed and ultrasonicated for 90 min to prepare g-CN/$SmFeO_3$ photocatalysts (Fig. 1). The composites were recovered by centrifugation and dried at 70°C before use. Composites with g-CN:$SmFeO_3$ weight ratios of 20:80, 50:50 and 80:20 were prepared.

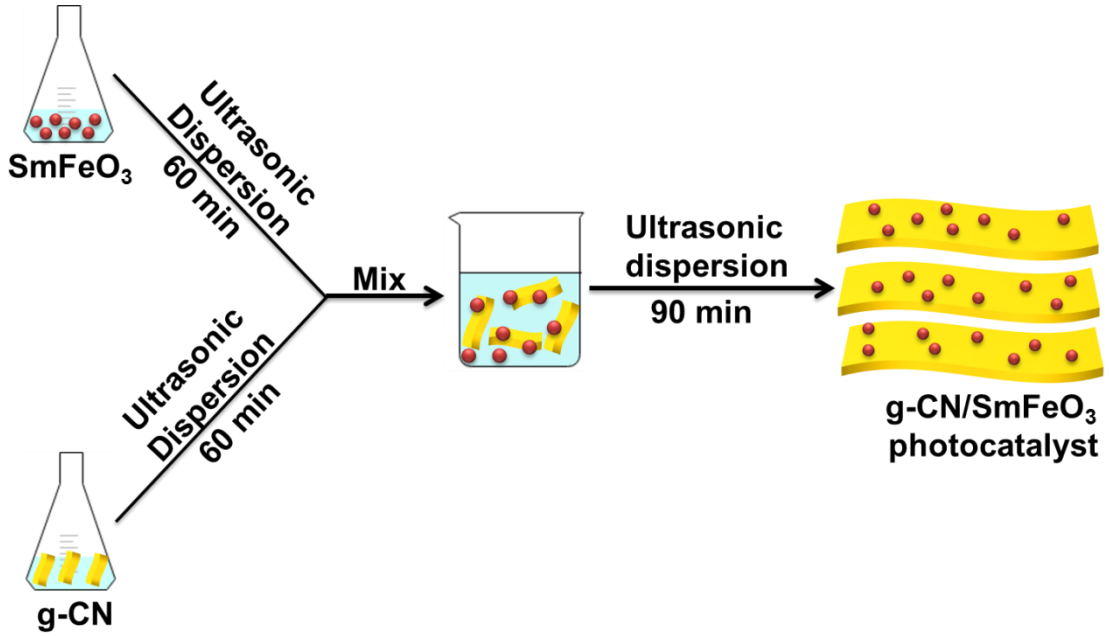

Fig. 1. Schematic representation of g-CN/$SmFeO_3$ composites synthesis.

The thermal stability and the weight percentage of g-CN in g-CN/$SmFeO_3$ composites were determined by TGA from room temperature to 1000°C at a heating rate of 10°C.min^{-1} (Fig. 2). For pure $SmFeO_3$, the weak weight loss (ca. 1.5%) originates from the removal of physisorbed water molecules. Pure g-CN is stable until ca. 550°C and shows a fast weight loss

from 585 to 722°C due to the combustion of g-CN under air atmosphere. The thermal stability of g-CN/$SmFeO_3$ composites is lower than that of pure g-CN and the burning of g-CN is observed at ca. 500°C, indicating that $SmFeO_3$ particles catalyze the decomposition of g-CN. The actual content in $SmFeO_3$ was determined from the remaining mass at 1000°C and was found to be of 78.6, 46.0 and 14.2% for g-CN/$SmFeO_3$ composites prepared with g-CN:$SmFeO_3$ ratios of 20:80, 50:50 and 80:20, respectively.

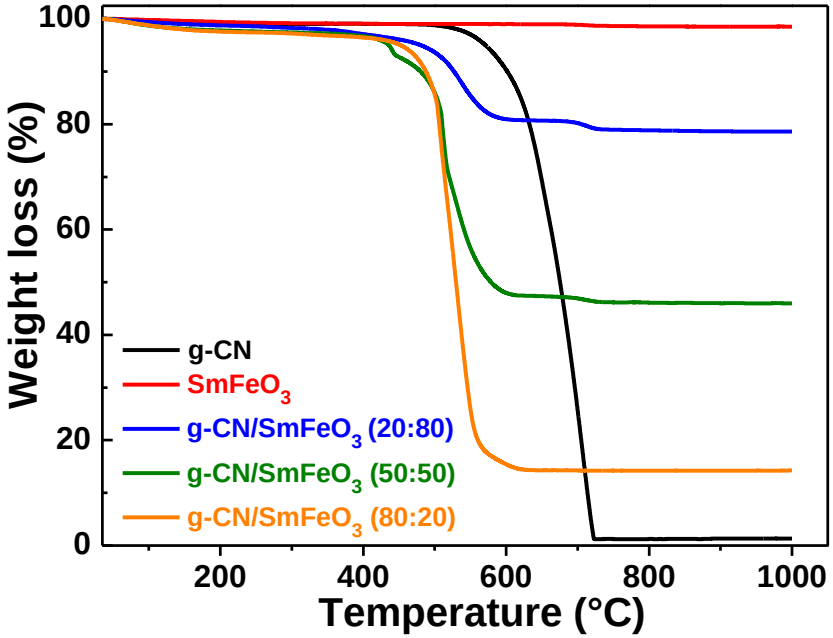

Fig. 2. TGA plots of bulk g-CN, $SmFeO_3$ and g-CN/$SmFeO_3$ composites.

XRD and FT-IR investigations were first carried out to elucidate the structure and the compositions of g-CN/$SmFeO_3$ composites. XRD patterns of the as-prepared $SmFeO_3$, g-CN and g-CN/$SmFeO_3$ samples are shown in Fig. S1 and Fig. 3a. For pure $SmFeO_3$, the XRD pattern recorded after calcination at 600°C shows the orthorhombic phase of $SmFeO_3$. All peaks can be assigned to the perovskite structure (space group Pbnm) (JCPDS No 74–1474) (Fig. S1) and no impurities like Sm_2O_3 or Fe_2O_3 could be detected [36]. For bulk g-CN, two diffraction peaks located at 27.48 and 13.19° corresponding to the (002) plane (inter-layer stacking of the conjugated aromatic system) and to the (100) plane (in-plane structural packing motif of tri-s-triazine units), respectively, were observed [9, 10, 37]. For the g-CN/$SmFeO_3$ composites, the coexistence of $SmFeO_3$ and g-CN phases can be clearly seen and

the intensities of the signals related to g-CN increase with the loading in g-CN. The crystal phases of $SmFeO_3$ and g-CN were not affected by the mixing-ultrasonication method used to assemble these materials.

The FT-IR spectrum of $SmFeO_3$ shows two strong absorption bands located at 412 cm^{-1} and 540 cm^{-1} attributed to the octahedral stretching mode of Fe-O and to the deformation vibration mode of O-Fe-O bonds, respectively (Fig. 3b) [38]. The FT-IR spectrum further confirms the phase purity of $SmFeO_3$. For pure g-CN, the peaks located at 1227, 1390, 1464 and 1627 cm^{-1} originate from C-N stretchings [39,40], while the signal at 808 cm^{-1} is associated to the characteristic breathing mode of s-triazine units [40]. The weak band between 3100 and 3300 cm^{-1} corresponds to the N-H stretching vibration. The peaks of g-CN and $SmFeO_3$ appear in all the spectra of the g-CN/$SmFeO_3$ composites and further confirm their successful association.

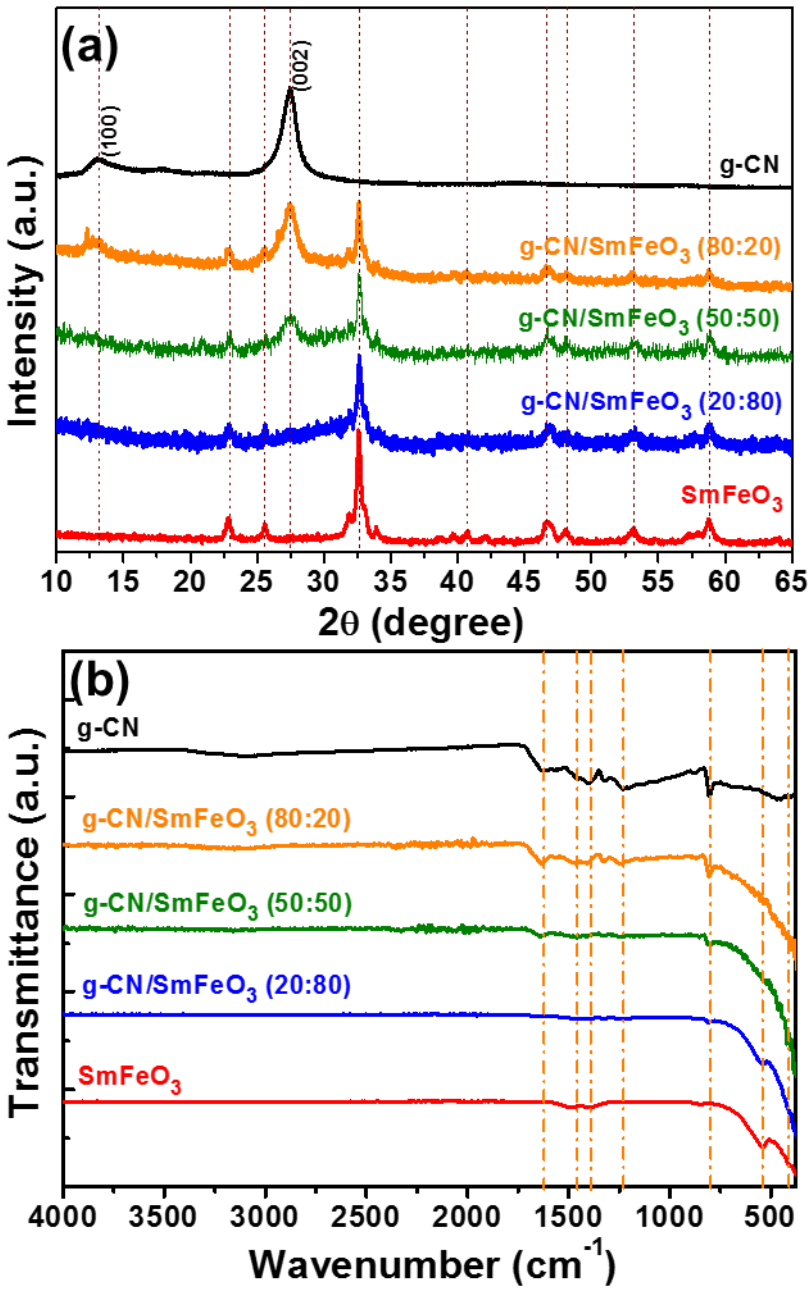

Fig. 3. (a) XRD patterns and (b) FT-IR spectra of bulk g-CN, $SmFeO_3$ and g-CN/$SmFeO_3$ photocatalysts.

To investigate the surface composition and chemical state of the elements present in the photocatalysts, XPS measurements were conducted (Fig. 4). As can be seen from the survey spectrum (Fig. 4a), only the C, N, Sm, Fe and O elements were detected. The high resolution XPS spectrum of C 1s can be deconvoluted into three signals. The main peak located at

288.17 eV can be assigned to sp^2-hybridized C atoms in the N-C=N bonds of the aromatic system [41]. The weaker signals at 284.68 and 286.08 eV originate from adventitious carbon (C-C and C=C bonds) and from C-O bonds, respectively (Fig. 4b). The N 1s XPS signal shows three components located at 398.77, 400.32 and 401.38 eV corresponding to sp^2-hybridized nitrogen (C-N=C), to tertiary nitrogen N-$(C)_3$ and to free amino functions, respectively (Fig. 4c) [42]. The Sm $3d_{5/2}$ peak and the Fe $2p_{3/2}$ peak are located at 1084.12 and 711.83 eV, respectively, and confirm that Sm and Fe are both present in the +3 oxidation state (Fig. 4d-e). Both signals are shifted to higher binding energies compared to pure $SmFeO_3$, which suggests a strong association between g-CN and $SmFeO_3$ [43,44]. Finally, the O 1s high resolution spectrum can be fitted with two components located at 530.77 and 533.02 eV corresponding to Sm-O and Fe-O bonds in the $SmFeO_3$ lattice and to carbonate species adsorbed at the surface of the photocatalyst, respectively (Fig. 4f) [33].

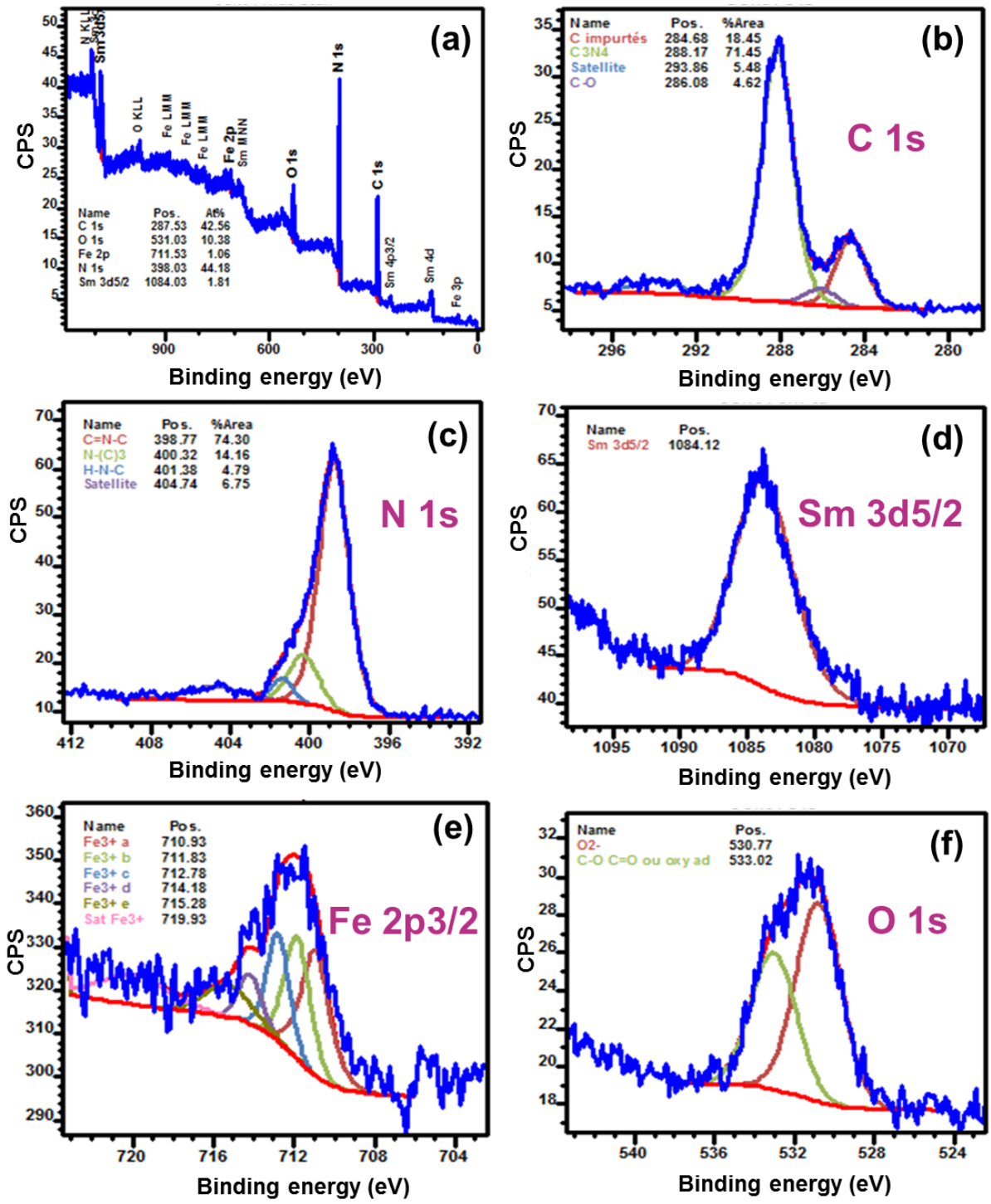

Fig. 4. (a) XPS survey spectrum of the g-CN/$SmFeO_3$ (80/20) composite and high resolution XPS spectra of (b) C 1s, (c) N 1s, (d) Sm 3d, (e) Fe 2p and (f) O 1s.

The morphology, the structure and the composition of $SmFeO_3$ and g-CN/$SmFeO_3$ materials were investigated by SEM and TEM. SEM and TEM images show that $SmFeO_3$ is composed of clusters of particles with an average diameter of 19 ± 5 nm (Fig. 5a and Fig. 6a and the inset) while exfoliated g-CN is composed of thin nanosheets with sizes varying of a few hundred of

nm to a few µm as shown in Fig. S2. $SmFeO_3$ particles clusters are well-dispersed and embedded into wrinkled g-CN sheets (Fig. 5b-d). The SEM- associated EDX analyses confirm the presence of C, N, Sm, Fe and O elements in g-CN/$SmFeO_3$ composites (Fig. S3).

TEM analyses also show that $SmFeO_3$ particles are coated by g-CN sheets (Fig. 6b-d). The surface heterojunction formed between g-CN and $SmFeO_3$ should favor the charge separation and transportation and thus the photocatalytic activity. Well-defined lattice fringes can be observed for $SmFeO_3$ on the HR-TEM images. The interplanar distances of 0.27 and 0.34 nm correspond to the (112) or (200) and (111) planes of orthorhombic $SmFeO_3$, respectively (fig. 6e-f). The selected area electron diffraction (SAED) patterns show diffraction rings corresponding to orthorhombic $SmFeO_3$ (insets of Fig. 6a-d), which agrees well with XRD results.

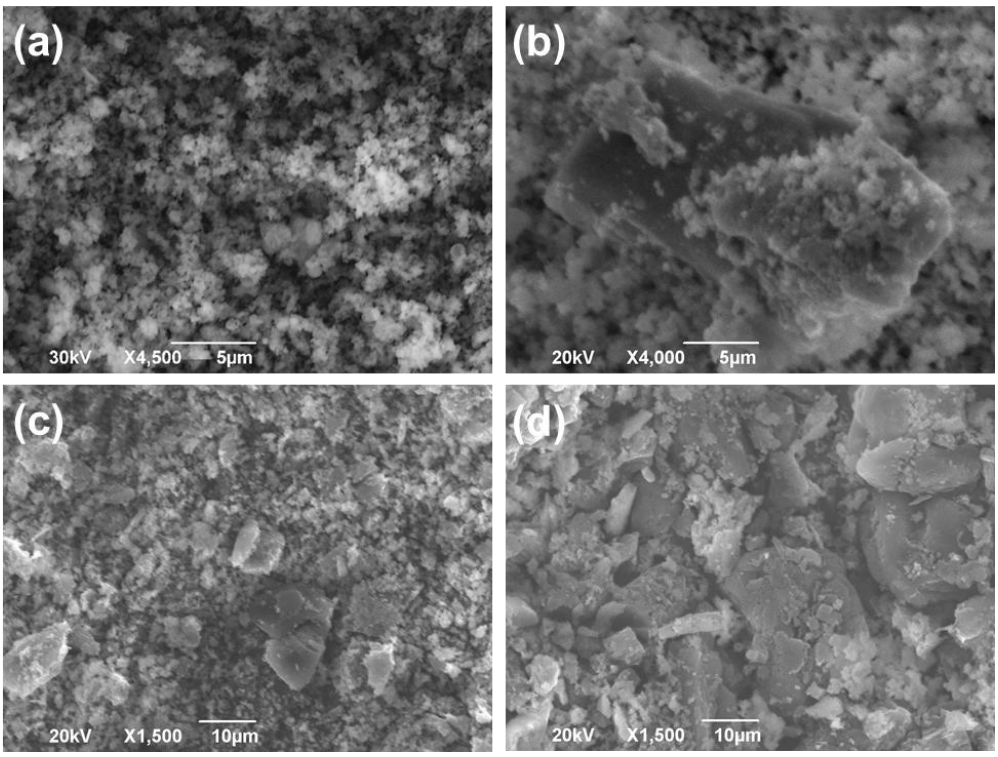

Fig. 5. SEM images of (a) $SmFeO_3$ and (b-d) g-CN/$SmFeO_3$ composites prepared with g-CN:$SmFeO_3$ ratios of 20:80, 50:50 and 80:20, respectively.

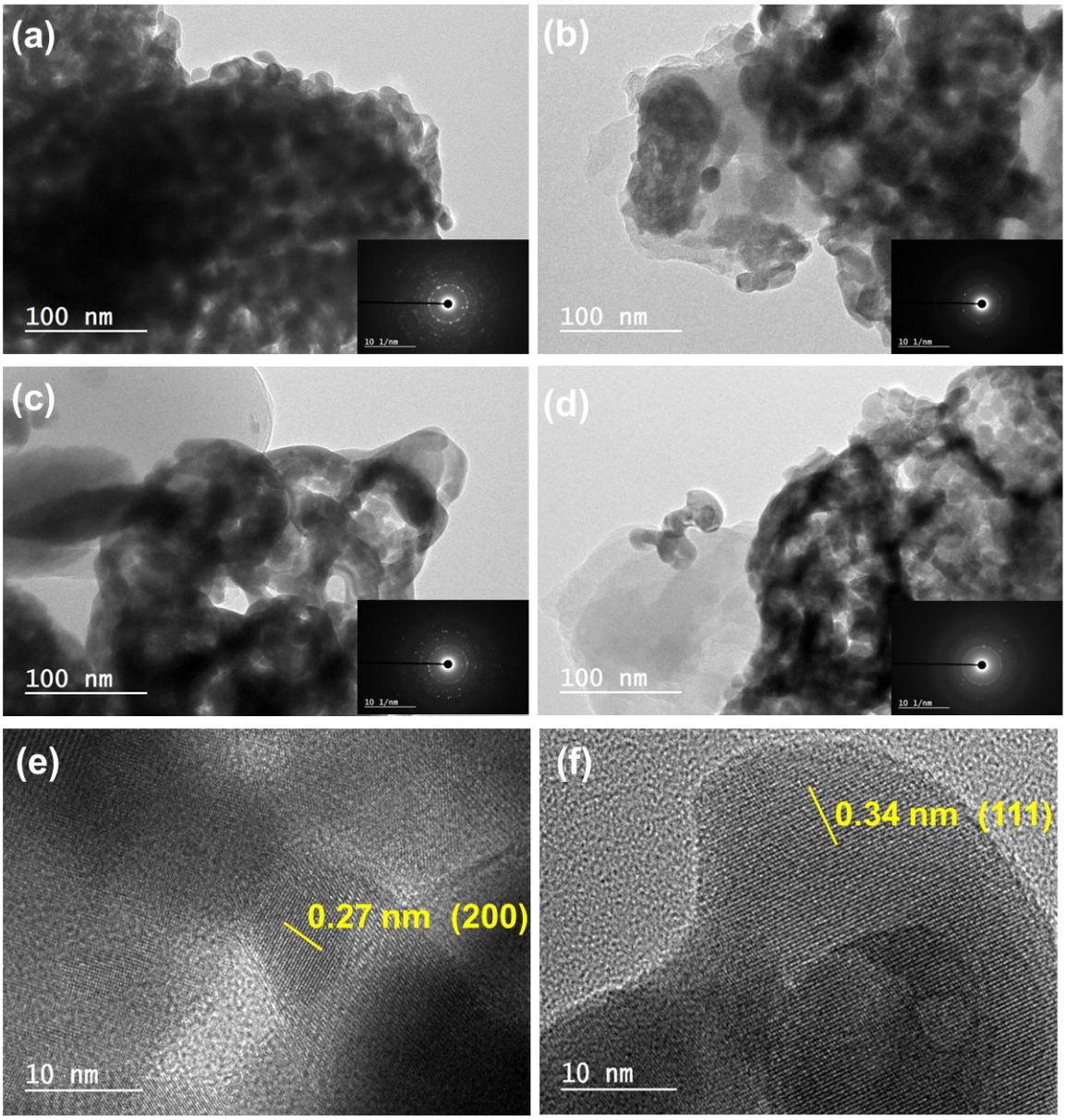

Fig. 6. TEM images of (a) $SmFeO_3$ and (b-d) g-CN/$SmFeO_3$ composites prepared with g-CN:$SmFeO_3$ ratios of 20:80, 50:50 and 80:20, respectively. The top inset of a is the size distribution and the bottom insets are the SAED patterns. (e-f) HR-TEM images of g-CN/$SmFeO_3$ composites.

The specific surface area of bulk and exfoliated g-CN, of $SmFeO_3$ and of the g-CN/$SmFeO_3$ (80:20) composite were determined via N_2 adsorption-desorption experiments conducted at 77 K (Fig. 7). All samples exhibit type IV isotherms according to the IUPAC classification. The BET specific surface area measured for pure $SmFeO_3$ is 25.4 $m^2.g^{-1}$. After association with g-CN, the specific surface area of g-CN/$SmFeO_3$ (80:20) composite decreased to 18.84 $m^2.g^{-1}$, likely due to the blocking of some active sites of $SmFeO_3$ by g-CN. Noteworthy is that these

values are significantly higher than those determined for bulk and exfoliated g-CN (5.80 and 11.17 $m^2.g^{-1}$, respectively). The H3 type hysteresis loops observed in the 0.9 to 1.0 relative pressure range indicate the presence of slit-like pores, which should provide more surface-active sites and thus improve the photocatalytic activity.

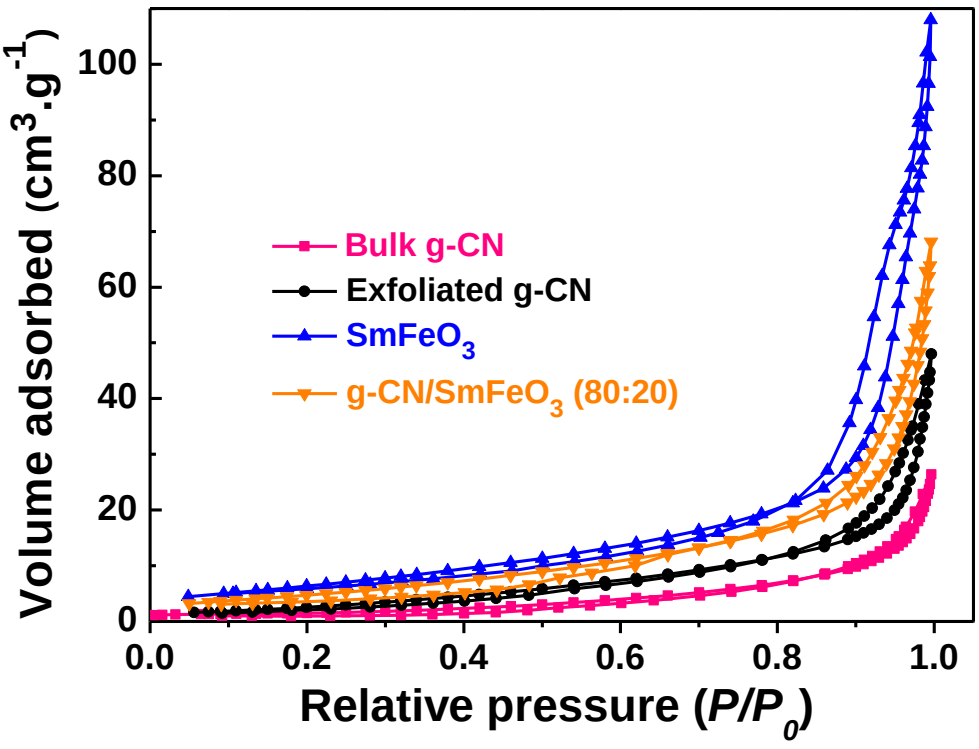

Fig. 7. N_2 adsorption-desorption isotherms of bulk and exfoliated g-CN, $SmFeO_3$ and of the g-CN/$SmFeO_3$ (80:20) composite.

3.2 Optical properties

The UV-visible absorption spectra of $SmFeO_3$, g-CN and the g-CN/$SmFeO_3$ photocatalysts are given in Fig. 8a. The bandgap energy (Eg) of the samples was determined by the equation $\alpha h\upsilon = B(h\upsilon - Eg)^2$, where α, h, υ, Eg and B are the absorption coefficient, the Planck constant, the light frequency, the bandgap energy and a constant, respectively (Fig. 8b). $SmFeO_3$ nanoparticles absorb light over the whole visible region due to their low bandgap energy (2.01 eV). The absorption of perovskite-type oxides like $SmFeO_3$ at high wavelengths

originates from the electronic transition from the valence band to the conduction band (O 2p → Fe 3d) [45]. The absorption edge of pure g-CN is at ca. 450 nm, which corresponds to a bandgap of 2.75 eV, value in good accordance with previous reports [9, 10, 46]. The UV-visible absorption in the 300-600 nm region of g-CN/$SmFeO_3$ composites decreases with the g-CN content due to its lower bandgap. Simultaneously, the bandgap energy increases from 2.01 to 2.65 eV. All g-CN/$SmFeO_3$ composites exhibit a significantly higher absorption in the visible range than g-CN which should improve their photocatalytic activity under visible light irradiation.

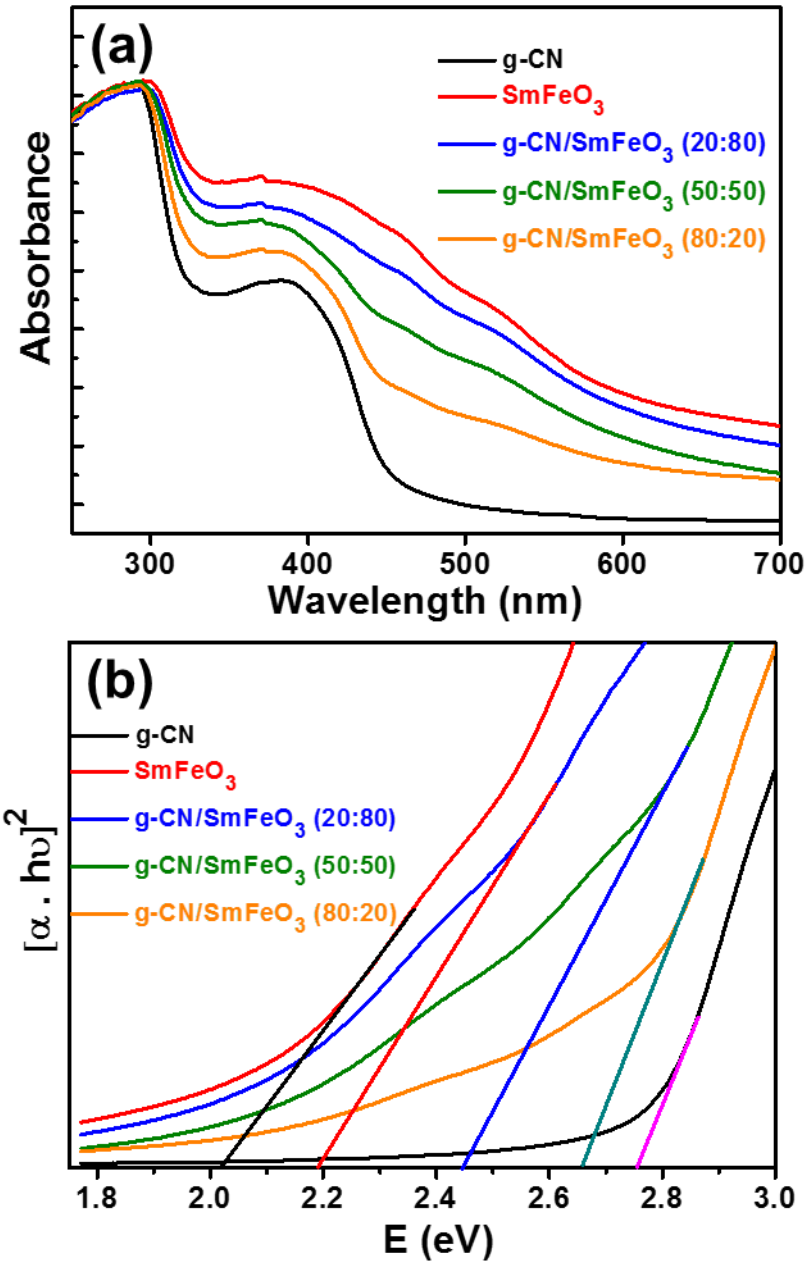

Fig. 8. (a) UV-visible absorption spectra of bulk g-CN, $SmFeO_3$ and g-CN/$SmFeO_3$ photocatalysts and (b) the corresponding $[\alpha hv]^2$ vs photon energy plots.

3.3 Photocatalytic activity

The surface charge of g-CN, $SmFeO_3$ and g-CN/$SmFeO_3$ (80:20) photocatalysts was determined by zeta potential measurements (Fig. S4). The point of zero charge (pzc) for g-CN is of 4.21, value in good agreement with previous reports [47]. The pzc of the g-CN/$SmFeO_3$

(80:20) catalyst increased to 5.02 due to the high pzc value of pure $SmFeO_3$ (8.82). These results indicate that the g-CN/$SmFeO_3$ (80:20) composite is positively-charged at neutral pH, which should facilitate the degradation of anionic pollutants that will strongly adsorb at its surface via electrostatic interactions.

The photocatalytic activity of g-CN/$SmFeO_3$ composites was first evaluated in the degradation of the negatively-charged Orange II dye (10 $mg.L^{-1}$) under visible light irradiation (intensity of 15 $mW.cm^{-2}$) and at neutral pH. Before irradiation, the solution was stirred in the dark for 30 min to reach the physisorption equilibrium of the dye. The percentage of Orange II adsorbed increases with the loading in g-CN in g-CN/$SmFeO_3$ composites (from 8 to 15%) (Fig. 9a), which agrees with zeta potential measurements. Preliminary experiments show that the photolysis of Orange II in the absence of catalyst is negligible. As can be seen from Fig. 9a, pure $SmFeO_3$ exhibits no photocatalytic activity, likely due to the high recombination rate of photogenerated electron-hole pairs, while ca. 92% of the dye was bleached after 150 min irradiation using g-CN. The photocatalytic activity of g-CN/$SmFeO_3$ composites increases with the loading in g-CN. The highest activity was obtained for the g-CN/$SmFeO_3$ (80:20) catalyst with Orange II being decomposed at 97% after 150 min irradiation. The photodegradation was found to be a pseudo-first-order kinetic process expressed by $\ln(C_0/C) = kt$ where C_0 and C are the concentrations of Orange II at time 0 and t, respectively, and k is the apparent first-order rate constant. The rate constants determined for g-CN and g-CN/$SmFeO_3$ 20:80, 50:50 and 80:20 catalysts are 1.6, 0.5, 1.3 and 1.9×10^{-2} min^{-1} and further confirm that the g-CN/$SmFeO_3$ (80:20) composite exhibits the highest performance for the degradation of Orange II (Fig. S5). The physical mixing of g-CN and $SmFeO_3$ (wt ratio of 80/20) yields a photocatalyst exhibiting an activity slightly lower than that of pure g-CN ($k = 1.45$ min^{-1}), which further accounts for the enhanced charge separation when g-CN and $SmFeO_3$ are brought in contact by ultrasonication. The high activity observed for g-CN/$SmFeO_3$ (80:20) composite likely originates from its weak bandgap of 2.65 eV that allows to produce more photo-generated charge carriers than g-CN under visible light irradiation, from the p-n junction that promotes the separation of the charge carriers (*vide infra*) and from its relatively high specific surface area (18.84 $m^2.g^{-1}$) that affords more active sites for the degradation of Orange II.

The photodegradation of tetracycline hydrochloride (TC), an antibiotic widely used against bacteria-related diseases, was also investigated [48]. TC is a refractory pollutant and only poorly decomposed via conventional oxidative or biological processes [49]. Since TC exists in its zwitterionic form at neutral pH [50], no adsorption of TC was observed at the surface of g-CN or g-CN/$SmFeO_3$ (80:20) catalysts during the 30 min of stirring in the dark (Fig. 9b). After 180 min of visible light irradiation, 97% of TC was degraded using g-CN/$SmFeO_3$ (80:20) or (50:50) composites while only 77% of TC was decomposed using pure g-CN or the g-CN/$SmFeO_3$ (20:80) composite. As previously, the photocatalytic activity of $SmFeO_3$ is modest and only 18% degradation could be achieved. The photodegradation data were fitted to the pseudo-first-order model and the k values determined for g-CN and g-CN/$SmFeO_3$ (80:20), (50:50) and (20:80) catalysts are 0.85×10^{-2}, 1.88×10^{-2} min^{-1}, 1.83×10^{-2} min^{-1} and 0.81×10^{-2} min^{-1}, respectively (Fig. S6).

The performances of the g-CN/$SmFeO_3$ (80:20) composite are better than those of g-CN-based catalysts recently developed for the degradation of TC (P- and S-doped g-CN, C-doped g-CN, WO_3/g-CN/Bi_2O_3 or Ag_3PO_4/AgBr/g-CN) [51-54]. The photodegradation yield is of 70-85% after ca. 1 h irradiation using a light intensity of 100 $mW.cm^{-2}$ and the irradiation time could even be reduced to 25 min when using a light intensity of 160 $mW.cm^{-2}$. The lower rate observed in this study for the degradation of TC is related to much lower intensity irradiation used (25 $mW.cm^{-2}$) .

The stability of the g-CN/$SmFeO_3$ (80:20) photocatalyst was evaluated in six consecutive experiments using Orange II and TC as pollutants (see Fig. 9c and Fig. S7 for the results obtained with Orange II and TC, respectively). After each reaction, the photocatalyst was recovered by centrifugation and reused without any washing or drying in the next run. As can be seen, a slight decrease of the photocatalytic performance for Orange II removal from 97 to 82% was observed after the six cycles, indicating that the g-CN/$SmFeO_3$ composite exhibits a good stability and thus a high potential for practical applications. The slight decrease in activity observed after six reuses may originate from the adsorption of by-products formed during the degradation of the dye and remaining at the surface of the catalyst. Similar results were obtained using TC (decrease in activity from 97 to 88% after the 6^{th} reuse). The high stability of the g-CN/$SmFeO_3$ (80/20) composite was further confirmed

by SEM and XRD experiments in which no significant differences were observed between the as-prepared and the reused photocatalyst (Fig. S8).

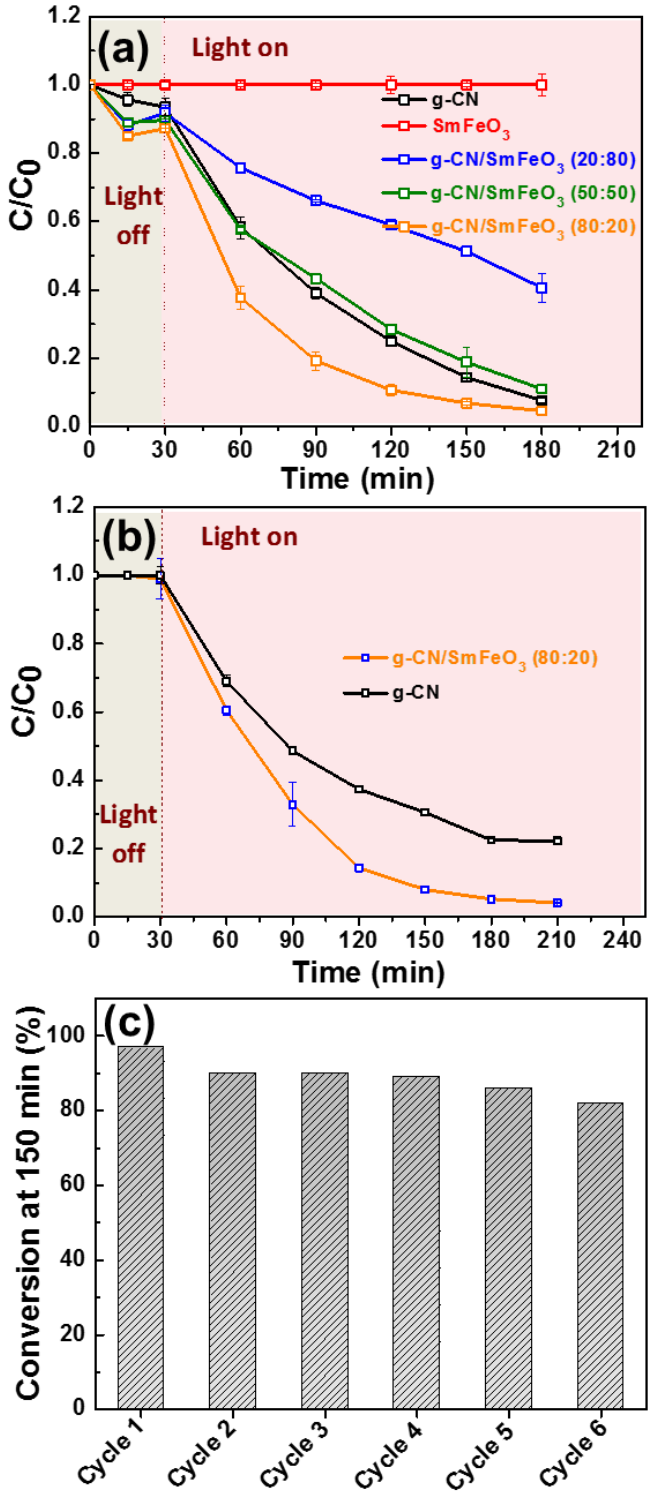

Fig. 9. Concentrations changes of (a) Orange II and (b) tetracycline hydrochloride under visible light irradiation (15 $mW.cm^{-2}$) using g-CN, $SmFeO_3$ or g-CN/$SmFeO_3$ composites as

photocatalysts. (c) Conversion of Orange II after 150 min irradiation in six consecutive cycles using the g-CN/$SmFeO_3$ (80:20) photocatalyst.

3.4 Influence of pH on the photodegradation

As the surface charge of the photocatalyst, the band edge position of its components and the charge of the pollutant depend on pH, it is of high importance to evaluate its influence on the catalytic activity [9]. A series of experiments were conducted by adjusting the pH of the Orange II solution to 4.5, 6, 7.5, 9 and 11 using 0.1 M HCl or NaOH before the adsorption phase. Fig. S9a presents the kinetics of the photodegradation vs pH using the g-CN/$SmFeO_3$ (80:20) catalyst. The adsorption of the dye on the catalyst surface is more pronounced at pH 4.5 (ca. 18%) due to the strong electrostatic interactions between the positively-charged catalyst surface (pzc = 5.02) and the negatively-charged dye. The dark-adsorption of the dye decreases with pH increase and almost no adsorption was observed at pH 11 due to the strong electrostatic repulsion between the dye (pK_a naphthol = 10.6) with the catalyst surface. As can be seen in Fig. S9b, the highest photocatalytic activity was observed at pH 4.5 ($k = 2.1\ 10^{-2}\ min^{-1}$) and Orange II was completely degraded in 150 min under visible irradiation. The degradation rates significantly decrease at pH 6, 7.5 and 9 ($k = 1.9\times10^{-2}$, 1.3×10^{-2} and $10^{-2}\ min^{-1}$, respectively) and the lowest kinetic was observed at pH 11 ($k = 0.02\times10^{-2}\ min^{-1}$).

3.5 Mechanism

To evaluate the contributions of the various active species in the photodegradation of Orange II, trapping experiments were conducted using 1,4-benzoquinone (p-BQ), tert-butanol (t-BuOH), EDTA and DMSO as scavengers of superoxide ($O_2^{\bullet-}$) radicals, hydroxyl ($^{\bullet}OH$) radicals, holes and electrons, respectively (all experiments were performed at pH 6.7 which corresponds to the pH of the Orange II solution without any additives) [9, 10, 17]. As can be seen from Fig. 10a and S10, $O_2^{\bullet-}$ radicals and holes play a major role in the decomposition of the dye (only 46 and 50% degradation after 150 min irradiation when adding p-BQ and EDTA, respectively) while the addition of electrons and $^{\bullet}OH$ radicals scavengers only slightly restrained the photodegradation. Similar experiments were also conducted using TC as pollutant and at pH 4.4 which corresponds to the pH of the starting TC

solution (Fig. S11). The same active species were found to be involved in the degradation of TC but holes have the major role (43 and 73% degradation after 150 min irradiation when adding EDTA and p-BQ, respectively). These experiments suggest that photogenerated electrons quickly react with O_2 molecules adsorbed at the surface of the photocatalyst to generate $O_2^{\bullet-}$ radicals, and thus preventing electrons to recombine with holes.

To further explore the photocatalytic mechanism, the separation efficiency of photogenerated electron-hole pairs was investigated by PL spectroscopy. Fig. 10b shows the PL emission spectra of g-CN, $SmFeO_3$ and of the g-CN/$SmFeO_3$ composites after excitation at 350 nm (the PL intensities g-CN and g-CN/$SmFeO_3$ were normalized to the actual g-CN weight in the photocatalysts). Two strong PL emissions centered at 438 and 460 nm can be observed for g-CN after excitation at 350 nm indicating a high recombination rate of photogenerated electron-hole pairs while $SmFeO_3$ is non-fluorescent. A marked decrease of the PL intensity is observed with the increase of the $SmFeO_3$ loading in the photocatalysts, indicating that the electron-hole recombination in g-CN is effectively impeded after coupling with $SmFeO_3$.

Photoelectrochemical measurements were further conducted to investigate the efficiency of the charge carrier separation in p-n heterostructured $SmFeO_3$/g-CN photocatalysts. Indeed, the photocurrent intensity is linked to the ability of a semiconductor to generate and transfer charge carriers under illumination [9, 10, 17]. Fig. 10c shows the transient photocurrent response curves of g-CN, $SmFeO_3$ and of g-CN/$SmFeO_3$ composites coated on a FTO electrode in several on-off cycles of visible light irradiation. A fast generation of photocurrent and a good reproducibility are observed for all samples upon illumination while the current intensity is almost close to 0 when light is turned off. Pure $SmFeO_3$ exhibits a low photocurrent (0.05 µA) while that measured for g-CN is significantly higher (0.33 µA). The photocurrent increases with the g-CN content in the composites and average values of 0.14, 0.40 and 0.51 µA were determined for 20:80, 50:50 and 80:20 g-CN/$SmFeO_3$ composites, respectively. The highest value obtained for the g-CN/$SmFeO_3$ (80:20) composite, ca. 1.6-fold higher than that of pure g-CN, comes from the synergetic effect between the charge separation efficiency and the high BET specific surface area of this sample, which agrees well with photocatalytic results.

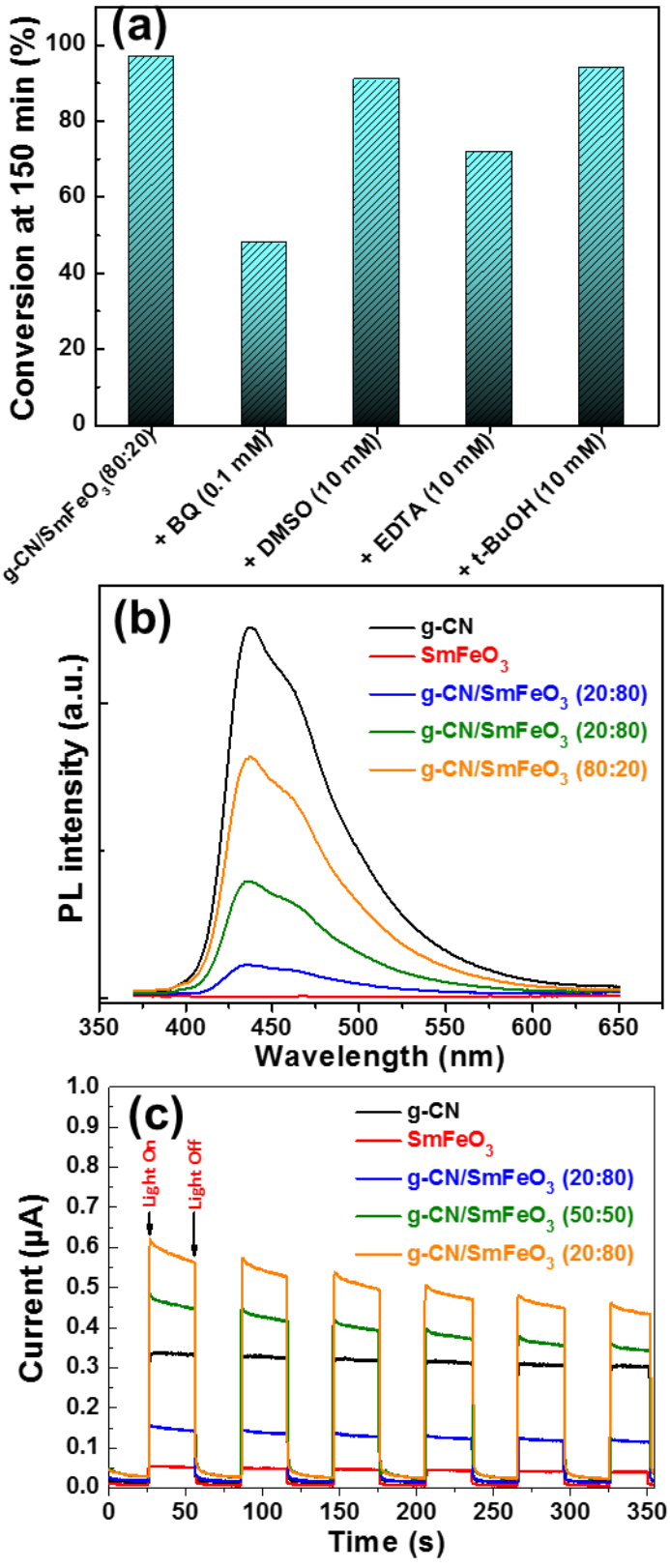

Fig. 10. (a) Photodegradations efficiencies of Orange II after 150 min irradiation over the g-CN/$SmFeO_3$ (80:20) catalyst when adding p-BQ, DMSO, EDTA and t-BuOH as scavengers (all

reactions were conducted at pH 6.7), (b) PL emission spectra and (c) transient photocurrent responses of g-CN, $SmFeO_3$ and g-CN/$SmFeO_3$ composites.

The energy bandgap of $SmFeO_3$ was calculated to be 2.01 eV (Fig. 8b). The band edge position of the conduction band (E_{CB}) and of the valence band (E_{VB}) of $SmFeO_3$ at the point of zero charge can be determined using the Mulliken electronegativity theory :

$$E_{CB} = \chi - E^e - 0.5\ Eg$$

where χ is the absolute electronegativity of $SmFeO_3$ (5.56 eV), E^e is the energy of free electrons on the hydrogen scale (ca. 4.5 eV vs NHE) and Eg is the bandgap energy [55]. For $SmFeO_3$, the calculated ECB and EVB values are 0.05 and 2.06 eV, respectively. The χ value for g-CN is 4.42 eV and E_{CB} and E_{VB} values were determined to be -1.34 and 1.41 eV, respectively.

Under visible light irradiation, both $SmFeO_3$ and g-CN can be photo-activated to generate electrons and holes. As depicted in Fig. 11a, E_{CB}(g-CN) is more negative that E_{CB}($SmFeO_3$) and photoexcited electrons in the CB of g-CN can easily transfer to the lower energy CB of $SmFeO_3$ due to the p-n junction established between $SmFeO_3$ and g-CN and the inner electric field generated. However, these electrons cannot reduce O_2 into $O_2^{\bullet-}$ radicals since the CB edge potential of $SmFeO_3$ (0.05 eV) is more positive than the redox potential of the $O_2/O_2^{\bullet-}$ couple (-0.18 eV vs NHE) (Fig. 11a). These data are inconsistent with the scavenging experiments previously described which show that $O_2^{\bullet-}$ radicals play an important role in the degradation of Orange II and TC. Therefore, reactions mediated by the g-CN/$SmFeO_3$ photocatalyst likely occur via a Z-scheme mechanism (Fig. 11b) [56]. The interfacial junction between g-CN and $SmFeO_3$ allows electrons in the CB of $SmFeO_3$ to flow to the VB of g-CN and recombine with holes. The CB edge potential (-1.34 eV) of g-CN is more negative than the redox potential of the $O_2/O_2^{\bullet-}$ couple and electrons in the CB of g-CN react with O_2 to give $O_2^{\bullet-}$ radicals that can oxidize the pollutants into CO_2 and H_2O. The holes in the VB of $SmFeO_3$ cannot oxidize H_2O into $^{\bullet}OH$ radicals as the VB edge potential (+2.06 eV) is more

negative than the redox potential of the $^{\bullet}OH/H_2O$ couple (+2.32 eV vs NHE). However, these holes can directly oxidize Orange II or TC into the degradation products. The Z-scheme mechanism allows to inhibit the recombination of charge carriers, this increases the lifetime of electron-hole pairs and improves the photocatalytic activity of the g-CN/$SmFeO_3$ composite compared to pure g-CN. These results are in good agreement with trapping experiments which demonstrate that $O_2^{\bullet-}$ radicals and holes play a key role in the photodegradation mechanism.

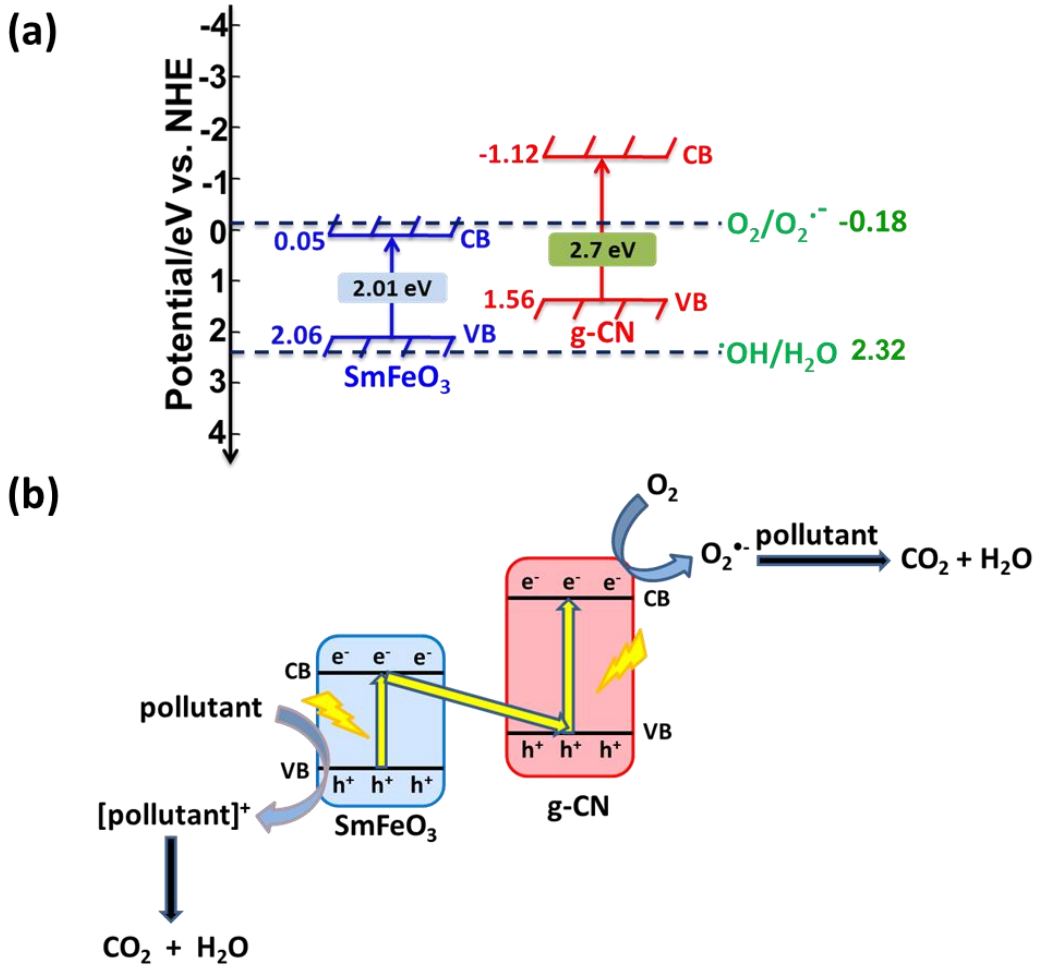

Fig. 11. (a) Band structure of the g-CN/$SmFeO_3$ photocatalyst and (b) schematic illustration of the delocalization of charge carriers and of the formation of reactive species involved in the photodegradation.

4. Conclusion

A series of heterostructured g-CN/$SmFeO_3$ photocatalysts was prepared via a mixing-ultrasonication process using perovskite $SmFeO_3$ nanoparticles with an average diameter of 19 nm and g-CN nanosheets as starting materials. The photocatalysts were characterized by various experimental techniques and their photocatalytic performance was evaluated in the degradation of the Orange II dye and tetracycline hydrochloride under visible light irradiation. The g-CN/$SmFeO_3$ (80:20) composite shows the highest photocatalytic activity and a high stability after six reuses. The high photocatalytic activity can be attributed to the interfacial n-p heterojunction between g-CN and $SmFeO_3$ which promotes an efficiency separation of the photogenerated electron/hole pairs and to the increased visible light absorption compared to pure g-CN. Trapping experiments of active species involved in the photodegradation shows that $O_2^{\bullet-}$ radicals and holes play the major role and a Z-scheme charge carrier transfer pathway is proposed for the mechanism. We expect that the g-CN/$SmFeO_3$ composites developed in this work can be of high interest for wastewater treatment, but also for other photocatalytic applications like hydrogen production.

Acknowledgments

This work has received the financial support from the Institut Carnot ICEEL.

Appendix A. Supplementary data

Supplementary data to this article can be found online at https:// doi.org/.

References

[1] [1] Wen J, Xie J, Chen X and Li X 2017 A review on g-C_3N_4-based photocatalysts *Appl. Surf. Sci.* **391** 72-123

[2] Masih D, Ma Y and Rohani S 2017 Graphitic C_3N_4 based noble-metal-free photocatalyst systems: A review *Appl. Catal. B: Environ.* **206** 556-88

[3] Mishra A, Mehta A, Basu S, Shetti N P, Reddy K R and Aminabhavi T M 2019 Graphitic carbon nitride (g-C_3N_4)-based metal-free photocatalysts for water splitting: A review *Carbon* **149** 693-721

[4] Fu J, Yu J, Jiang C and Cheng B 2018 g-C_3N_4-Based Heterostructured Photocatalysts *Adv. Energy Mater.* **8** 1701503

[5] Zhang C, Li Y, Shuai D, Shen Y, Xiong W and Wang L 2019 Graphitic carbon nitride (g-C_3N_4)-based photocatalysts for water disinfection and microbial control: a review *Chemosphere* **214** 462-79

[6] Zhang S, Gu P, Ma R, Luo C, Wen T, Zhao G, Cheng W and Wang X 2019 Recent developments in fabrication and structure regulation of visible-light-driven g-C_3N_4-based photocatalysts towards water purification: A critical review *Catal. Today* **335** 65-77

[7] Darkwah W K and Oswald K A Photocatalytic Applications of Heterostructure Graphitic Carbon Nitride: Pollutant Degradation, Hydrogen Gas Production (water splitting), and CO2 Reduction *Nanoscale Res. Lett.* **14** 234

[8] Mambo G and Mishra A K 2016 Graphitic carbon nitride (g-C_3N_4) nanocomposites: A new and exciting generation of visible light driven photocatalysts for environmental pollution remediation *Appl. Catal. B: Environ.* **198** 347-77

[9] Moussa H, Chouchene B, Gries T, Balan L, Mozet K, Medjahdi G and Schneider R 2018 Growth of ZnO Nanorods on Graphitic Carbon Nitride gCN Sheets for the Preparation of Photocatalysts with High Visible-Light Activity *ChemCatChem* **10** 4973-83

[10] Ben Abdelaziz M, Chouchene B, Balan L, Gries T, Medjahdi G, Ezzaouia H and Schneider R 2019 One pot synthesis of bismuth oxide/graphitic carbon nitride composites with high photocatalytic activity *Molecular Catal.* **463** 110–18

[11] Lu C, Zhang P, Jiang S, Wu X, Song S, Zhu M, Lou Z, Li Z, Liu F, Liu Y, Wang Y and Li Z 2017 Photocatalytic reduction elimination of UO_2^{2+} pollutant under visible light with metal-free sulfur doped g-C_3N_4 photocatalyst *Appl. Catal. B: Environ.* **200** 378-85

[12] Fu J, Zhu B, Jiang C, Cheng B, You W and Yu J 2017 Hierarchical porous O-doped g-C_3N_4 with enhanced photocatalytic CO_2 reduction activity *Small* **13** 1603938

[13] Huang J, Li D, Li R, Zhang Q, Chen T, Liu H, Liu Y, Lv W and Liu G 2019 An efficient metal-free phosphorus and oxygen co-doped g-C_3N_4 photocatalyst with enhanced visible light photocatalytic activity for the degradation of fluoroquinolone antibiotics *Chem. Eng. J.* **374** 242-53

[14] Li Z, Kong C and Lu G 2016 Visible photocatalytic water splitting and photocatalytic two-electron oxygen formation over Cu- and Fe-doped g-C_3N_4 *J. Phys. Chem. C* **120** 56-63

[15] Hu J, Zhang P, An W, Liu L, Liang Y and Cui W 2019 In-situ Fe-doped g-C_3N_4 heterogeneous catalyst via photocatalysis-Fenton reaction with enriched photocatalytic performance for removal of complex wastewater *Appl. Catal. B: Environ.* **245** 130-42

[16] Wang J C, Cui C X, Li Y, Liu L, Zhang Y P and Shi W 2017 Porous Mn doped g-C_3N_4 photocatalysts for enhanced synergetic degradation under visible-light illumination *J. Hazard. Mater.* **339** 43-53

[17] Ouedraogo S, Chouchene B, Desmarets C, Gries T, Balan L, Fournet R, Medjahdi G, Bayo K and Schneider R 2018 Copper octacarboxyphthalocyanine as sensitizer of graphitic carbon nitride for efficient dye degradation under visible light irradiation *Appl. Catal. A, Gen.* **563** 127–36

[18] Yang L, Huang J, Shi L, Cao L, Yu Q, Jie Y, Fai J, Ouyang H and Ye J 2017 A surface modification resultant thermally oxidized porous g-C_3N_4 with enhanced photocatalytic hydrogen production *Appl. Catal. B: Environ.* **204** 335-45

[19] Xu J, Wang Z and Zhu Y 2017 Enhanced visible-light-driven photocatalytic disinfection performance and organic pollutant degradation activity of porous g-C_3N_4 nanosheets *ACS Appl. Mater. Interfaces* **9** 27727-35

[20] Chen X, Shi R, Chen Q, Zhang Z, Jiang W, Zhu Y and Zhang T 2019 Three-dimensional porous g-C_3N_4 for highly efficient photocatalytic overall water splitting *Nano Energy* **59** 644-50.

[21] Kanhere P and Chen Z A review on visible light active perovskite-based photocatalysts *Molecules* **19** 19995-20022

[22] Wu Y, Wang H, Tu W, Liu Y, Tan Y Z, Yuan X and Chew J W 2018 Quasi-polymeric construction of stable perovskite-type $LaFeO_3$/g-C_3N_4 heterostructured photocatalyst for improved Z-scheme photocatalytic activity via solid p-n heterojunction interfacial effect *J. Hazard. Mater.* **347** 412-22

[23] Ibarra-Rodriguez L I, Huerta-Flores A M and Torres-Martinez L.M 2019 Facile synthesis of g-C_3N_4/$LaMO_3$ (M: Co, Mn, Fe) composites for enhanced visible-light-driven photocatalytic water splitting *Mater. Sci. Semicond. Process.* **103** 104643

[24] Zhou X, Chen Y, Li C, Zhang L, Zhang X, Ning X, Zhan L and Luo J 2019 Construction of $LaNiO_3$ nanoparticles modified g-C_3N_4 nanosheets for enhancing visible light photocatalytic activity towards tetracycline degradation *Sep. Purif. Technol.* **211** 179-88

[25] Rakibuddin M, Kim H and Khan M E 2018 Graphite-like carbon nitride (C_3N_4) modified N-doped $LaTiO_3$ nanocomposite for higher visible light photocatalytic and photo-electrochemical performance *Appl. Surf. Sci.* **452** 400-12

[26] Acharya S, Mansingh S and Parida K M The enhanced photocatalytic activity of g-C_3N_4-$LaFeO_3$ for the water reduction reaction through a mediator free Z-scheme mechanism *Inorg. Chem. Front.* **4** 1022-32

[27] Konstas P S, Konstantinou I, Petrakis D and Albanis T 2018 Synthesis, characterization of g-C_3N_4/$SrTiO_3$ heterojunctions and photocatalytic activity for organic pollutants degradation *Catalysts* **8** 554

[28] Kumar A, Schuerings C, Kumar S, Kumar A and Krishnan V 2018 Perovskite-structured $CaTiO_3$ coupled with g-C_3N_4 as a heterojunction photocatalyst for organic pollutant degradation *Beilstein J. Nanotechnol.* **9** 671-85

[29] Ismael M and Wu Y 2019 A facile synthesis method for fabrication of $LaFeO_3$/g-C_3N_4 nanocomposite as efficient visible-light-driven photocatalyst for photodegradation of RhB and 4-CP *New. J. Chem.* **43** 13783-93

[30] Behzadifard Z, Shariatinia Z and Jourshaboni M 2018 Novel visible light driven CuO/$SmFeO_3$ nanocomposite photocatalysts with enhanced photocatalytic activities for degradation of organic pollutants *J. Mol. Liquids* **262** 533-48

[31] Haye E, Capon F, Barrat S, Boulet P, Andre E, Carteret C and Bruyere S 2016 Properties of rare-earth orthoferrites perovskite driven by steric hindrance *J. Alloys Compds* **657** 631-38

[32] Tang P, Ni D, Cao F and Li B 2016 Microwave synthesis of nanoparticulate $SmFeO_3$ and Its characterization *J. Nanosci. Nanotechnol.* **16** 1151-54

[33] Mori M, Iwamoto Y, Asamoto M, Itagaki Y, Yahiro H, Sadaoka Y, Takase S, Shimizu Y, Yuasa M, Shimanoe K, Kusaba H and Teraoka Y 2008 Effect of preparation routes on the catalytic activity over $SmFeO_3$ oxide *Catal. Today* **139** 125-29

[34] Niu X, Li H and Liu G 2005 Preparation, characterization and photocatalytic properties of $REFeO_3$ (RE = Sm, Eu, Gd) *J. Mol. Cat. A: Chem.* **232** 89-93

[35] Maity R, Sakhya A P, Dutta A and Sinha T P 2019 Investigation of concentration dependent electrical and photocatalytic properties of Mn doped $SmFeO_3$ *Mater. Chem. Phys.* **223** 78-87

[36] Xu H, Hu X and Zhang L 2008 Generalized low-temperature synthesis of nanocrystalline rare-earth orthoferrites $LnFeO_3$ (Ln) La, Pr, Nd, Sm, Eu, Gd) *Cryst. Growth Des.* **8** 2061-65

[37] Yan S C, Li Z S and Zou Z G 2009 Photodegradation performance of g-C_3N_4 fabricated by directly heating melamine *Langmuir* **25** 10397-401

[38] Rao G V S and Rao C N R 1970 Infrared and electronic spectra of rare earth perovskites: Ortho-Chromites, -Manganites and -Ferrites *Appl. Spectrosc.* **24** 436-45

[39] Chai B, Peng T, Mao J, Lia K and Zan L 2012 Graphitic carbon nitride (g-C_3N_4)-Pt-TiO_2 nanocomposite as an efficient photocatalyst for hydrogen production under visible light irradiation *Phys. Chem. Chem. Phys.* **14** 16745-52

[40] Wang Y, Shi R, Lin J and Zhu Y 2011 Enhancement of photocurrent and photocatalytic activity of ZnO hybridized with graphite-like C_3N_4 *Energy Environ. Sci.* **4** 2922-29

[41] Lin Q, Li L, Liang S, Liu M, Bi J and Wu L 2015 Efficient synthesis of monolayer carbon nitride 2D nanosheet with tunable concentration and enhanced visible-light photocatalytic activities *Appl. Catal. B: Environ.* **163** 135-42

[42] Elbanna O, Fujitsuka M and Majima T 2017 g-C_3N_4/TiO_2 Mesocrystals composite for H_2 evolution under visible-light irradiation and its charge carrier dynamics *ACS Appl. Mater. Interfaces* **9** 34844-54

[43] Bukhari S M and Giorgi J B Effect of cobalt substitution on thermal stability and electrical conductivity of $Sm_{0.95}Ce_{0.05}FeO_{3-\delta}$ in oxidizing and reducing conditions *Solid State Ion.* **181** 392-401

[44] Asamoto M, Horada N, Iwamoto Y, Yamaura H, Sadaoka Y and Yahiro H 2009 Catalytic activity of multi-metallic perovskite-type oxide prepared by the thermal decomposition of heteronuclear cyano complex, $Sm[Fe_x Co_{1-x}(CN)_6] \cdot nH_2O$ *Top. Catal.* **52** 823-27

[45] Parida K M, Reddy K H, Martha S, Das D P and Biswal N 2010 Fabrication of nanocrystalline $LaFeO_3$: an efficient sol–gel auto-combustion assisted visible light responsive photocatalyst for water decomposition *Int. J. Hydrogen Energy* **35** 12161–68

[46] Xu J, Long K Z, Wang Y, Xue B and Li Y X 2015 Fast and facile preparation of metal-doped g-C_3N_4 composites for catalytic synthesis of dimethyl carbonate *Appl. Catal. A: Gen.* **496** 1-8

[47] Zhu B, Xia P, Ho W and Yu J 2015 Isoelectric point and adsorption activity of porous g-C_3N_4 *Appl. Surf. Sci.* **344** 188-95

[48] Palominos R A, Mondaca M A, Giraldo A, Penuela G, Perez-Moya M and Mansilla H D 2009 Photocatalytic oxidation of the antibiotic tetracycline on TiO_2 and ZnO suspensions *Catal. Today* **144** 100-5

[49] Wei X, Feng H, Li L, Gong J, Jiang K, Xue S and Chu P K 2020 Synthesis of tetragonal prismatic γ-In_2Se_3 nanostructures with predominantly {110} facets and photocatalytic degradation of tetracycline *Appl. Catal. B: Environ.* **260** 118218

[50] Hsu L C, Liu Y T, Syu C H, Huang M H, Tzou Y M and Teah H Y 2018 Adsorption of tetracycline on Fe (hydr)oxides: effects of pH and metal cation (Cu^{2+}, Zn^{2+} and Al^{3+}) addition in various molar ratios *R. Soc. Open Sci.* **5** 171941

[51] Jiang L, Yuan X, Zeng G, Chen X, Wu Z, Liang J, Zhang J, Wang H and Wang H 2017 Phosphorus- and Sulfur-Codoped g C_3N_4: Facile Preparation, Mechanism Insight, and Application as Efficient Photocatalyst for Tetracycline and Methyl Orange Degradation under Visible Light Irradiation *ACS Sustainable Chem. Eng.* **5** 5831-41

[52] Panneri S, Ganguly P, Mohan M, Nair B N, Peer Mohamed A A, Warrier K G and Hareesh U S 2017 Photoregenerable, Bifunctional Granules of Carbon-Doped g C_3N_4 as Adsorptive Photocatalyst for the Efficient Removal of Tetracycline Antibiotic *ACS Sustainable Chem. Eng.* **5** 1610-18

[53] Jiang L, Yuan X, Zeng G, Liang J, Chen X, Yu H, Wang H, Wu Z, Zhang J and Xiong T 2018 In-situ synthesis of direct solid-state dual Z-scheme WO_3/g-C_3N_4/Bi_2O_3 photocatalyst for the degradation of refractory pollutant *Appl. Catal. B: Environ.* **277** 376-85

[54] Yu H, Wang D, Zhao B, Lu Y, Wang X, Zhu S, Qin W and Huo M 2020 Enhanced photocatalytic degradation of tetracycline under visible light by using a ternary photocatalyst of Ag_3PO_4/AgBr/g-C_3N_4 with dual Z-scheme heterojunction *Sep. Purif. Technol.* **237** 116365

[55] Xu Y and Schoonen M A A 2000 The absolute energy positions of conduction and valence bands of selected semiconducting minerals *Am. Mineral.* **85** 543-56

[56] Li Y, Xia Y, Liu K, Ye K, Wang Q, Zhang S, Huang Y and Liu H 2020 Constructing Fe-MOF-Derived Z-scheme Photocatalysts with Enhanced Charge Transport: Nanointerface and Carbon Sheath Synergistic Effect *ACS Appl. Mater. Interfaces* **12** 25494-502